Ceramics International xxx (xxxx) xxx

Contents lists available at ScienceDirect

Ceramics International

journal homepage: www.elsevier.com/locate/ceramint

Ag-sensitized Tb^{3+}/Yb^{3+} codoped silica-zirconia glasses and glass-ceramics: Systematic and detailed investigation of the broadband energy-transfer and downconversion processes

Francesco Enrichi [a,b,d,*], Elti Cattaruzza [b], Pietro Riello [b], Giancarlo C. Righini [c], Alberto Vomiero [b,d]

[a] CNR-ISP, Institute of Polar Sciences, National Research Council, Via Torino 155, 30172, Mestre-Venezia, Italy
[b] Department of Molecular Sciences and Nanosystems, Ca' Foscari University of Venice, Via Torino 155, 30172, Mestre-Venezia, Italy
[c] CNR-IFAC, Nello Carrara Institute of Applied Physics, National Research Council, Via Madonna del Piano 10, 50019, Sesto Fiorentino, Firenze, Italy
[d] Division of Materials Science, Department of Engineering Sciences and Mathematics, Luleå University of Technology, 971 87, Luleå, Sweden

ARTICLE INFO

Keywords:
Rare-earth ions
Ag multimers
Tb/Yb
Down-conversion
Glass-ceramics
Silica-zirconia

ABSTRACT

Various studies report that Tb^{3+}/Yb^{3+} co-doped materials can split one UV or 488 nm (visible) photon in two near infrared (NIR) photons at 980 nm by an energy-transfer process involving one Tb^{3+} and two Yb^{3+} ions. Additionally, it was demonstrated that Ag multimers can provide an efficient optical sensitizing effect for rare earth ions (RE^{3+} ions), resulting in a broadband enhanced excitation, which could have a significant technological impact, overcoming their limited spectral absorptions and small excitation cross sections. However, a systematic and detailed investigation of the down-conversion process enhanced by Ag nanoaggregates is still lacking, which is the focus of this paper. Specifically, a step by step analysis of the energy-transfer quantum-cutting chain in Ag-exchanged Tb^{3+}/Yb^{3+} co-doped glasses and glass-ceramics is presented. Moreover, the direct Ag-Yb^{3+} energy-transfer is also considered. Results of structural, compositional, and optical characterizations are given, providing quantitative data for the efficient broadband Ag-sensitization of Tb^{3+}/Yb^{3+} quantum cutting. A deeper understanding of the physical processes beneath the optical properties of the developed materials will allow a wiser realization of more efficient energy-related devices, such as spectral converters for silicon solar cells and light-emitting devices (LEDs) in the visible and NIR spectral regions.

1. Introduction

Spectral down-conversion, also known as quantum-cutting, is a process that splits the energy of one photon in two or more photons. This process may occur in rare-earth doped materials thanks to the number and distribution of available energy levels for rare-earth-ions [1] and it has many possible applications, from photovoltaics (PV) to lighting and photonics. In the field of silicon solar cells, down-conversion could provide a significant boost of the solar cell's efficiency by transforming one ineffective UV–Vis photon in two or more photons that can be exploited by the PV solar cell [2,3], whose peak absorptions falls typically in the red or near-IR.

In this context, the Tb^{3+}/Yb^{3+} rare-earth pair has been extensively investigated and reported in literature [4–13]. Indeed, Yb^{3+} emission in the NIR around 980 nm (about 1.27 eV) is close to the silicon bandgap, which corresponds to 1120 nm for c-Si (Eg = 1.11 eV at 300 K) and therefore it could be efficiently converted in electricity. However, the absorption and emission properties of Yb^{3+} ions are related to transitions between only two energy levels: $^2F_{7/2}$ (ground state) and $^2F_{5/2}$ (excited state). Therefore, Yb^{3+} is not able to absorb UV or visible light and co-doping with Tb^{3+} ions is commonly used. Indeed, Tb^{3+} can act as sensitizer both in the UV and in the blue spectral region for Yb^{3+}, with the additional possibility of doubling the number of photons: the decay from the $^5D_4$ excited state of Tb^{3+} to the ground state can occur non-radiatively by the simultaneous excitation of two Yb^{3+} ions, and consequently can result in the final emission of two lower energy photons at 980 nm (as shown in Figure S1).

Our recent studies on this subject focused on the optimization of the host material and rare-earth concentrations [14]. A comparison between glasses (G) and glass-ceramics (GC), made by a homogeneous

* Corresponding author. CNR-ISP, Institute of Polar Sciences, National Research Council, Via Torino 155, 30172, Mestre-Venezia, Italy.
E-mail address: francesco.enrichi@cnr.it (F. Enrichi).

https://doi.org/10.1016/j.ceramint.2021.03.107
Received 1 January 2021; Received in revised form 2 March 2021; Accepted 11 March 2021
Available online 16 March 2021

distribution of nanocrystals within an amorphous medium, highlighted the better optical performances of the latter for RE-doping. It has been reported that RE-ions tend to be segregated into the crystalline matrix inclusions [15–17], with better spectroscopic properties, higher solubilities and lower phonon energies, which lead to a reduced non-radiative recombination rates with respect to the glassy counterpart. Our studies demonstrated the possibility to obtain 160% down-conversion efficiency in silica-hafnia (70%–30%) glasses and up to 190% in the corresponding glass-ceramics prepared at higher temperature. This very high down-conversion efficiency, close to the maximum theoretical limit of 200%, would make this material extremely interesting for increasing the efficiency of solar cells, but the narrow absorption bandwidths and the small excitation cross sections of RE^{3+} ions (Tb^{3+} in this specific case) are major limiting factors for the full exploitation of their potentials, making Tb^{3+}/Yb^{3+} down-conversion almost unpractical for real PV applications. To overcome these limits, the addition of proper sensitizers for RE^{3+} ions is an efficient and viable strategy. In this respect, silver multimers have known luminescent properties [18–21]. Unlike silver nanoparticles, which can be used in PV solar cells for their plasmonic effects [22–25], but have the drawback of introducing significant absorption losses [26,27], single ions or multimers can act as broadband efficient downshifters [28] or sensitizers [29–32] due to a non-radiative energy-transfer (ET) process.

In principle, silver multimers can be used as antennas for Tb^{3+} [33] ions and Yb^{3+} ions [34,35], as we recently demonstrated. Furthermore, recent works by Lin et al. [36] and by ourselves [37] reported that molecular-like Ag aggregates act as sensitizers for energy-transfer in Tb^{3+}/Yb^{3+} ions and make possible a broadband enhanced excitation. However, a detailed systematic analysis of the Ag-sensitized down-conversion process is still lacking, and it would be of major importance both from a fundamental understanding of the physics and for unveiling its potential for applications. Such analysis is the focus of this paper, which deals with the step-by-step investigation of the quantum-cutting energy-transfer chain in Ag exchanged Tb^{3+}/Yb^{3+} co-doped glasses and glass-ceramics (Fig. 1). Each link in the chain from UV absorption to NIR emission has been deeply analysed: Ag-doping alone (step I), Ag–Tb^{3+} interaction (step II), Ag–Tb^{3+}-Yb^{3+} system (step III). Moreover, the direct Ag-Yb^{3+} energy-transfer has also been investigated.

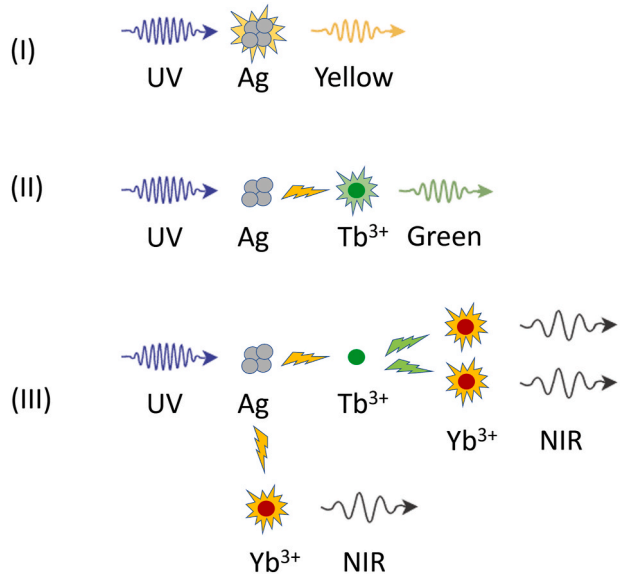

Fig. 1. Scheme of the broadband quantum-cutting process involving Ag aggregates and Tb^{3+}/Yb^{3+} ions, investigated in detail in this paper through a step-by-step PL analysis: (I) Ag only, (II) Ag–Tb^{3+}, (III) Ag–Tb^{3+}-Yb^{3+}. The possibility of Ag-Yb^{3+} interaction is also considered.

2. Material and methods

Undoped, Tb-doped (1 mol.%), Yb-doped (4 mol.%) and Tb–Yb co-doped (1 mol.% Tb – 4 mol.% Yb) films of nominal molar composition 70 SiO_2 – 30 ZrO_2 and additional 5 mol.% Na_2O were prepared by sol–gel technique and deposited by dip-coating (Figure S2). Tetraethyl orthosilicate $Si(OC_2H_5)_4$ (TEOS) and zirconium propoxide $Zr(OC_3H_7)_4$ (ZPO) were used as precursor for silica and zirconia, respectively. TEOS was dissolved in ethanol (EtOH) and hydrolized with H_2O and HCl (TEOS: HCl: H2O: EtOH = 1 : 0.01: 2: 25, Sol.Si). For Tb-doped, Yb-doped and Tb–Yb co-doped samples, 1 mol.% terbium nitrate $TbNO_3$ or/and 4 mol.% ytterbium nitrate $YbNO_3$ were added to the solution (Sol.Si-RE) and then left stirring for 1 h. In the meanwhile, ZPO was mixed with acetylacetone (Acac) and ethanol (ZPO: Acac: EtOH = 1 : 0.5: 50, Sol.Zr) and sodium acetate was dissolved in methanol (60 mg/ml, Sol.Na). The deposition solution has been obtained by mixing Sol.Si-RE with Sol.Zr and adding dropwise Sol.Na at room temperature. The solution has been left stirring at room temperature overnight for 16 h.

Multi-layer films have been deposited on silica substrates by dipping. Each layer was annealed in air at 700 °C for 3 min. A final heat treatment in air at 700 °C (glass, G) or 1000 °C (glass-ceramic, GC) for 1 h was performed after the deposition of the last single layer. The typical thickness of each single layer after heat treatment was about 40 nm. By this process we realized 10 layers crack-free films with a total thickness of about 400 nm.

Undoped, singly doped and co-doped (1 mol.% Tb – 4 mol.% Yb) G and GC films deposited on pure silica slides were realized (G0, G1, G4, G5 corresponding to undoped, Tb-doped, Yb-doped and Tb/Yb co-doped respectively). In order to introduce silver in the films, $Ag^+ \leftrightarrow Na^+$ ion-exchange [38] was performed by immersing the samples in a molten salt bath (1 mol.% $AgNO_3$ in $NaNO_3$) at 350 °C for 1 h. Ag-exchanged samples were indicated as G*X*-A (with X = 0, 1, 4, 5 corresponding to the RE^{3+} doping amount). After the ion exchange process, the samples followed a post-exchange heat treatment for 1 h at 380 °C or 430 °C in air, to investigate the possibility of migration and aggregation of the metal ions. Ag-exchanged and annealed samples were indicated as G*X*-B (380 °C) and G*X*-C (430 °C) following the same meaning as before.

Compositional, structural and optical characterization of the films were obtained by Rutherford Backscattering Spectrometry (RBS), X-Ray Diffraction (XRD), Transmission Electron Microscopy (TEM), UV–Vis–NIR transmission and Photoluminescence Spectroscopy.

RBS was carried out using a 2.0 MeV and 2.2 MeV $4He^+$ beam at 160° backscattering angle in IBM geometry. RUMP code was used for the analysis of the experimental spectra [39]. The conversion from areal density (the natural unit of measurement for RBS) to film thickness is based on a molar density of the film equal to a weighted average between silica (2.00 g cm^{-3}) and zirconia (5.68 g cm^{-3}), according to the nominal stoichiometric composition of the matrix (70 SiO_2 – 30 ZrO_2), confirmed by the RBS analysis.

XRD measurements for crystal phase identification were done at room temperature by an X'Pert PRO diffractometer (Panalytical). A Cu anode equipped with Ni filter was used as radiation source (Kα radiation, λ = 1.54056 Å). Diffractograms were collected both in Bragg-Brentano geometry and in grazing incidence, using a step-by-step scan mode in the 2θ range 10°–100°, with a scanning step of 0.05° and counting time of 30 s/step. Nanocrystal size was determined by Line Broadening Analysis (LBA), in particular by using the Warren-Averbach method [40].

TEM characterization was carried out by a Jeol JEM-3010 with an LaB6 cathode and high resolution pole pieces, equipped with an energy-dispersive X-ray spectrometer Oxford Instruments ISIS Series 300. The instrument was operated at 300 kV in bright field mode.

UV–Vis–NIR transmission spectra in the 200–1000 nm range were measured by an Agilent 8453 UV–Visible spectrophotometer.

Photoluminescence excitation (PLE), emission (PL) and time-resolved spectra in the visible and NIR range were recorded by an

Edinburgh Instruments FLS980 Photoluminescence Spectrometer. A continuous-wave xenon lamp or a microsecond-pulsed xenon flashlamp were used as excitation sources for steady-state or time-resolved measurements, respectively. The excitation wavelength was selected by a double-grating monochromator. The light emitted from the sample was also collected by a double-grating monochromator and recorded by a photon counting R928P PMT cooled at −20 °C (visible range) or by a R5509-73 PMT cooled at −80 °C (NIR range). Time-resolved PL decays were recorded in multi-channel-scaling (MCS) mode.

3. Results

3.1. Compositional characterization, structural analysis and UV–Vis–NIR transmission

The general label of each sample, like for example "G1-C", reports its structure (G = glass; GC = glass-ceramic), the nominal rare-earth concentration (0 = undoped; 1 = Tb 1%; 4 = Yb 4%; 5 = Tb 1% Yb 4%), any possible Ag-doping and annealing (A = Ag-exchanged; B = Ag-exchanged and 380 °C annealing; C = Ag-exchanged and 430 °C annealing).

The elemental composition was studied by RBS (Fig. 2). The analysis confirmed for all the samples the expected silica (70%) and zirconia (30%) composition. Since Tb and Yb edges in RBS are very close, the analysis did not allow to distinguish between them individually in the co-doped samples. However, the rare-earth molar concentration in singly doped Tb (1%) (G1 and GC1) and Yb (4%) (G4 and GC4) as well as their total amount in the co-doped samples (5%) (G5 and GC5) were perfectly confirmed. Moreover, the flat in-depth profiles clearly indicated a good compositional homogeneity and uniformity of the sol-gel deposition process.

RBS analysis on $Ag^{+}\leftrightarrow Na^{+}$ ion-exchanged samples (GX-A and GCX-A), both before and after annealing at 380 °C (GX-B and GCX-B) or 430 °C (GX-C and GCX-C), was also useful for evaluating the concentration profile of silver in the deposited films. The results show that glasses (G) allow a significantly higher Ag introduction than glass-ceramics (GC). Ag-concentration in as-exchanged G0-A sample is about 5.5 mol.% close to the surface and 3 mol.% inside the film, while GC0-A sample exhibits almost the same features, but with lower Ag-concentration between 2 mol.% (at surface) and 1.5 mol.% (inner part of the film). The analysis of Tb-doped samples report a uniform and flat Ag profile, with a constant value of 5.5 mol.% for G and 3 mol.% for GC. The dependence of ion-exchanged Ag concentration on the presence of the rare earth, both in terms of local amount and distribution profile within the matrix, seems to indicate an increased mobility of Ag in the doped matrix. It can be inferred that the presence of dopants like Tb^{3+} in the network may induce modifications and arrangements of the network. It is well-known that the ion-exchange process is extremely sensitive to several local parameters [41], as a competition between the diffusion process, which depends (a) on the local composition via the mobility and on the alkali behaviour, and (b) on the aggregation process, which depends on the local Ag concentration and on the

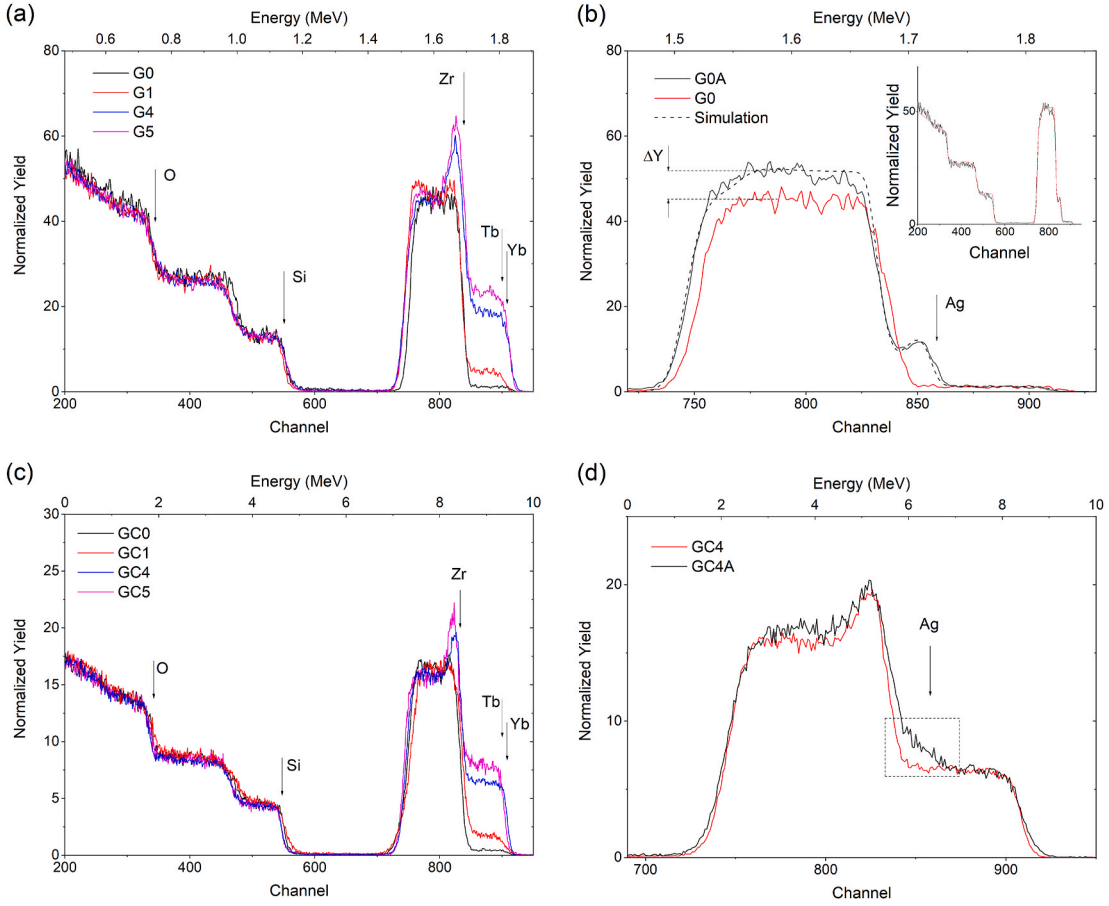

Fig. 2. Elemental depth profiling through RBS. (a) RBS spectra of the G-series, illustrating the presence of the silica-zirconia layer doped with different concentrations of rare earths. (b) High energy region of the RBS spectrum highlighting the signal from Zr before and after Ag doping. The presence of Ag is responsible for the difference in yield ΔY for the two spectra. Inset: experimental spectrum of the sample G0A (black) and RUMP code simulation (red). (c) RBS spectra of the GC-series, illustrating the presence of the silica-zirconia layer doped with different concentrations of rare earths. (d) RBS spectra of the sample GC4 before and after Ag doping. The dashed rectangle highlights the presence of Ag in the sample GC4-A The surface edges of O, Si, Zr, Ag, Tb and Yb are reported in the various panels. (For interpretation of the references to colour in this figure legend, the reader is referred to the Web version of this article.)

thermodynamics.

Furthermore, the diffusion of Ag upon thermal annealing is very different in the G and GC matrices. A much higher Ag mobility in the G matrix with respect to the GC matrix is clearly attested by RBS measurements. A significant Ag migration and accumulation up to 10 mol.% towards the surface with depletion of the inner layers can be observed in G samples (see, for instance, the surface Ag peak in Fig. 2(b)). On the contrary, the Ag profile in GC samples seems stable even for the highest 430 °C annealing temperature. This behaviour is reasonably attributed to the lower density, higher disorder, large presence of non-bridging oxygens and defectivity of the glass with respect to the multicrystalline glass-ceramic, being known that the structural properties strongly affect the diffusion processes. Indeed, as a general discussion, the diffusion coefficient, D, can be estimated through the Stokes-Einstein equation, Eqn. (1).

$$D = \frac{k_B T}{6\pi\mu R} \quad (1)$$

where T is the temperature, μ is the viscosity of the material, and R the radius of the diffusing particles (Ag atoms or ions in the present case). In a glass, the viscosity μ is dependent on the temperature, decreasing exponentially $\sim \exp(-bT)$, where b is a proper coefficient. Under these conditions, the "annealing temperature" is defined as the temperature at which $\log_{10} \mu = 13.4$, corresponding to a situation when all internal stresses are released, and a certain degree of mobility is allowed. For multicomponent glasses this value is typically about 500 °C, while for fused silica, for example, it can be as high as 1100 °C [42]. It follows that for GC samples, made of about 30% multi-crystalline ZrO_2, much lower average diffusion coefficients can be expected in comparison to the same glass composition, and at much higher temperatures. This holds in particular at 430 °C annealing conditions. From a different point of view, inside the GC matrix the diffusion coefficient is much higher in the amorphous silica interconnected network than inside the crystalline zirconia inclusions, therefore the path for Ag to go from one point to another, following the amorphous silica phase, is much longer, due to the numerous crystalline islands. This could explain the observed differences of Ag mobility in the two materials.

The XRD analyses of the synthesized G and GC samples before $Ag^+ \leftrightarrow Na^+$ ion-exchange are reported in Fig. 3(a), confirming the transition from an amorphous phase (G) to a glass-ceramic composite, containing crystalline ZrO_2 nanocrystals (GC) when the annealing temperature is raised from 700 °C to 1000 °C. Moreover, ZrO_2 tetragonal-phase nanocrystals were detected in the undoped and Tb-doped GC samples (GC0 and GC1), while cubic-phase nanocrystals were observed for Yb-doped and Tb/Yb co-doped samples (GC4 and GC5), attested by the different shape of the observed reflection peaks, especially those at $2\theta \approx 35.5°$ (200) and $2\theta \approx 75°$ (400) (Fig. 3(b)). Indeed, these reflections exhibit a single peak in the cubic phase, while they split in two components in the tetragonal phase. Unusual relative intensities of the observed diffraction peaks may be due to a preferential orientated growth of the zirconia nanocrystals along the [110] direction, as supported by comparing the reflections in Theta-2Theta geometry with the ones in grazing incidence geometry (Fig. 3(c)). For GC samples, the zirconia nanocrystal size was determined by Line Broadening Analysis (LBA) [40]. The calculated mean crystallite size was about 14 nm for tetragonal zirconia (GC0 and GC1 samples) and about 12 nm for cubic zirconia (GC4 and GC5 samples), with a broad distribution from 5 nm to 25 nm (see example in Fig. 3(d, e)).

After $Ag^+ \leftrightarrow Na^+$ ion exchange the XRD pattern of both G and GC samples did not reveal any Ag precipitate, even after annealing at the highest 430 °C temperature.

The structural properties of zirconia nanocrystals have been widely studied in literature. Bulk zirconia adopts a monoclinic crystal structure at room temperature, and it transforms to tetragonal (1170 °C) and cubic (2370 °C) at higher temperatures. However, the high surface energy of nanocrystalline size particles and/or the addition of dopants to the structure are crucial aspects for the stabilization of the tetragonal and cubic phase even at room temperature. Examples are the well-known yttria stabilized zirconia (YSZ) and the use of other trivalent or quadrivalent dopants like Ca, Ce, Fe, Ga, Gd, Ge, Nb, Sc [43–46]. Furthermore, novel orthorhombic phase stabilization was recently reported by Ta doping [47]. Therefore, the observed phase stabilization in GC samples can be reasonably due to a combination of different factors, including the size of the zirconia nanocrystals, the nature of the dopant ions and the amount of doping, keeping into account that this amount may be significantly increased from the nominal average doping by the fact that RE^{3+} ions tend to be incorporated in the nanocrystals during the annealing process, as already observed in this article's introduction [15–17]. Furthermore, we may expect different spectroscopic properties

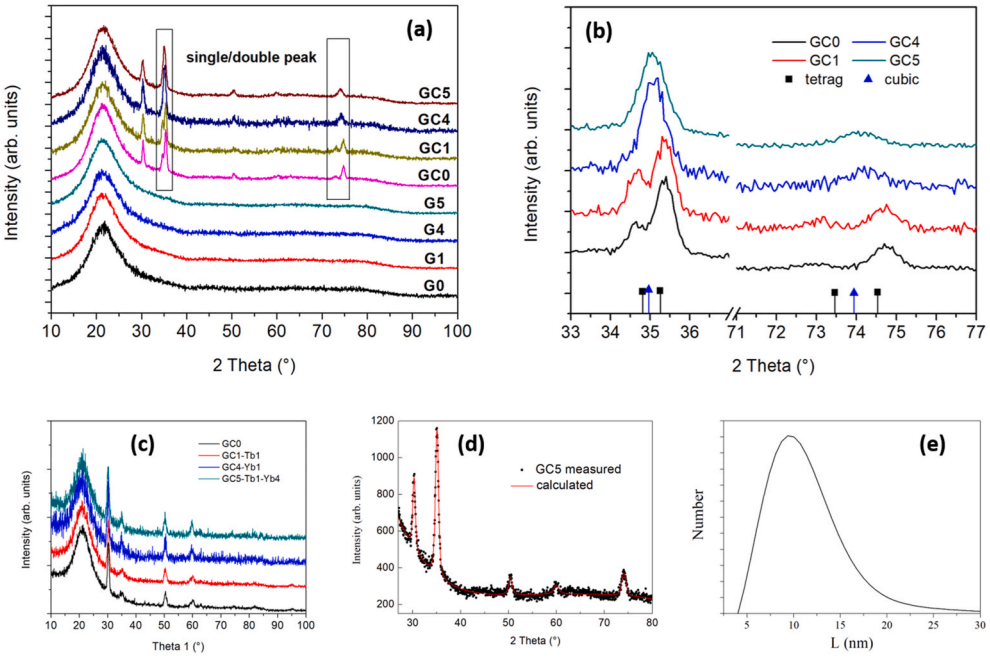

Fig. 3. XRD analysis on silica-zirconia-soda samples in Bragg-Brentano Theta-2Theta geometry (a). Only the final annealing at 1000 °C induce a phase separation between zirconia and silica (GC samples), otherwise the material is amorphous (G samples). The different shape of XRD reflections of GC samples (b) with or without Yb reveals a tetragonal (GC0 and GC1) or a cubic (GC4 and GC5) crystal phase, as detailed in the zoomed diffractogram regions. The different intensities of the peaks in grazing incidence geometry (c) compared to the Bragg-Brentano geometry suggest a preferential orientated growth of the zirconia nanocrystals along the [110] direction. As an example, the size fitting for GC5 sample (d) and the resulting nanocrystal size distribution (e), calculated by Line Broadening Analysis (LBA) [40] of XRD diffractogram is reported.

of Tb^{3+} and Yb^{3+} ions in GC materials depending on the actual phase, tetragonal or cubic, of the zirconia nanocrystals.

The prepared samples were also investigated by TEM, with the aim of both reporting the presence of zirconia nanocrystals and detecting the presence, if any, of silver clusters. As examples, TEM picture for the G1-A and GC1-A samples are reported in Fig. 4(a, b), confirming the presence of zirconia crystalline nanoparticles only in the glass-ceramic matrix, recognized by the typical crystal planes, variously distributed and oriented, and confirmed by Fast Fourier Transformation (FFT) analysis, reported in the insets of the pictures. Furthermore, Ag cluster precipitates were not detected in these images, but they were found in the superficial region of sample G1-C (Fig. 4(c)). EDAX analysis on GC1-A and GC1-C confirm the composition of zirconia nanocrystals and silver precipitates, reported in Fig. 4(d) and (e) respectively.

In view of their possible applications as downconverting films for solar cells, the optical transparency of the samples was tested. Figure S3 shows the optical transmission in the 200–1000 nm spectral range of undoped and Tb^{3+}/Yb^{3+} codoped glasses and glass-ceramics before and after Ag-exchange and annealing. Interference fringes are typical of transparent coatings whose thicknesses are some hundreds of nanometers and could be removed by antireflection treatments. For glasses, however, the baseline of the oscillations highlights a significant signal absorption which could be due to a lower densification, higher number of defects and, after Ag-exchange and annealing, to the possibility of silver aggregation and precipitation, as previously shown. Instead, excellent transparency can be noted, as good as the substrate alone, for the GC5 series, which are also the candidates for downconversion.

3.2. PL investigation of Ag aggregates (step I)

Since 1998, silver-doped silicate glasses have been reported for their broad PL excitation and emission bands under UV and near-UV illumination, in relation to the Ag luminescent species in the material [18–20]. More recently, this subject have seen a renewed interest for many potential applications such as, for example, solar cells [28] and white LEDs [48]. Moreover, it was shown that by proper stabilization they can be used as luminescent quantum clusters both in solids and in solutions [49]. With the possibility to reach very high quantum efficiencies up to about 90% in phosphosilicate glasses [50]. From the electron energy-level distribution it derives that isolated Ag^{+} ions emit typically in the 330–370 nm region, while Ag^{+}–Ag^{+} dimers emit around 430–450 nm. Moreover, a broad band from 550 to 650 nm and more appears for bigger clusters, like $(Ag_3)^{2+}$ trimers and small multimers.

As an example, Fig. 5 (top row) reports the PL emission (x-axis) – excitation (y-axis) maps of the glassy samples G0 (undoped glass), G0-A (Ag-exchanged) and G0-C (Ag-exchanged and annealed at 430 °C). The colour scales are the same in the three different images. The typical PL fingerprint of Ag aggregates can be clearly identified, with an excitation band from 320 nm to 380 nm peaked at 340 nm, and an emission band from 370 nm to 650 nm peaked at 410 nm. Additionally, by 280 nm excitation a charge transfer contribution related to energy-transfer from the matrix can be detected. The broad spectral emission indicates a wide range of silver species, which can span from Ag^{+} ions to aggregates. After annealing, the PL intensity is significantly reduced. To get a deeper insight into these issues and to compare G with GC material, PL excitation spectra, PL emission spectra and time-resolved PL in glass and glass-ceramic samples for the most significant wavelengths are reported in Fig. 5 (middle and bottom rows). The PL evolution of the Ag-exchanged samples with annealing temperature, in particular for 518 nm emission (PLE) and 330 nm excitation (PL) follows a different trend in G and GC samples. In G samples the PL intensity is decreasing with annealing and a slight red-shift can be observed in the shape of the PL emission. This can be reasonably attributed to the higher mobility of Ag in glasses, in agreement with RBS analysis. The Ag migration towards the surface and the higher density after annealing (from 5 mol.% to 10 mol.%) pushes the evolution of silver structures from dimers to multimers and bigger aggregates, which results in a lower number of emitting centres, together with a red-shifted photoluminescence. On the other hand, in the same measurement conditions (518 nm emission for PLE and 330 nm excitation for PL), the intensity is slightly increased in GC samples after annealing. Indeed, as attested by RBS, the Ag local concentration in glass-ceramics is stable with annealing, therefore the number and nature of the emitting centres is not changed. However, we can expect that the thermal treatment may have a favourable improvement of the silver surroundings, with possible reduction of non-radiative recombination defects and a recovery of the material quality. This explanation is further supported by PL lifetime evolution reported in Fig. 5. Indeed, PL lifetime is strongly related to the quality of the

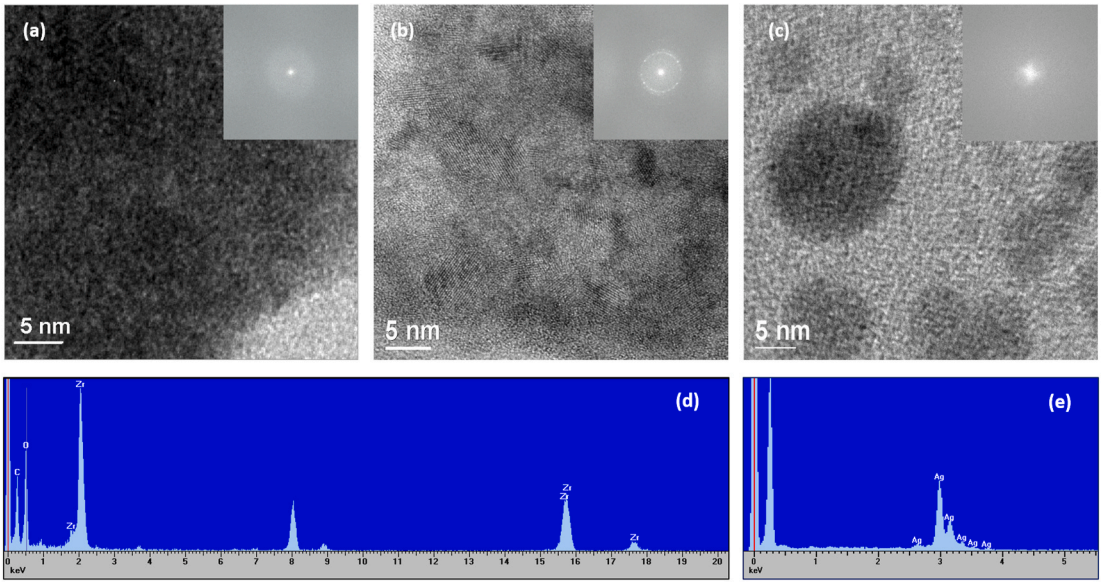

Fig. 4. TEM images of G1-A (a) and GC1-A (b) samples and the corresponding FFT analysis in the insets. Many distributed ZrO_2 nanocrystals can be detected only in the glass-ceramic matrix, with almost random orientations. Ag clusters were not detected in these samples. After annealing at 430 °C, Ag clusters were detected in the glass G1-C sample (c). EDAX analysis on GC1-A (d) confirms the composition of zirconia nanocrystals, while EDAX analysis on G1-C (e) confirms the composition of silver precipitates.

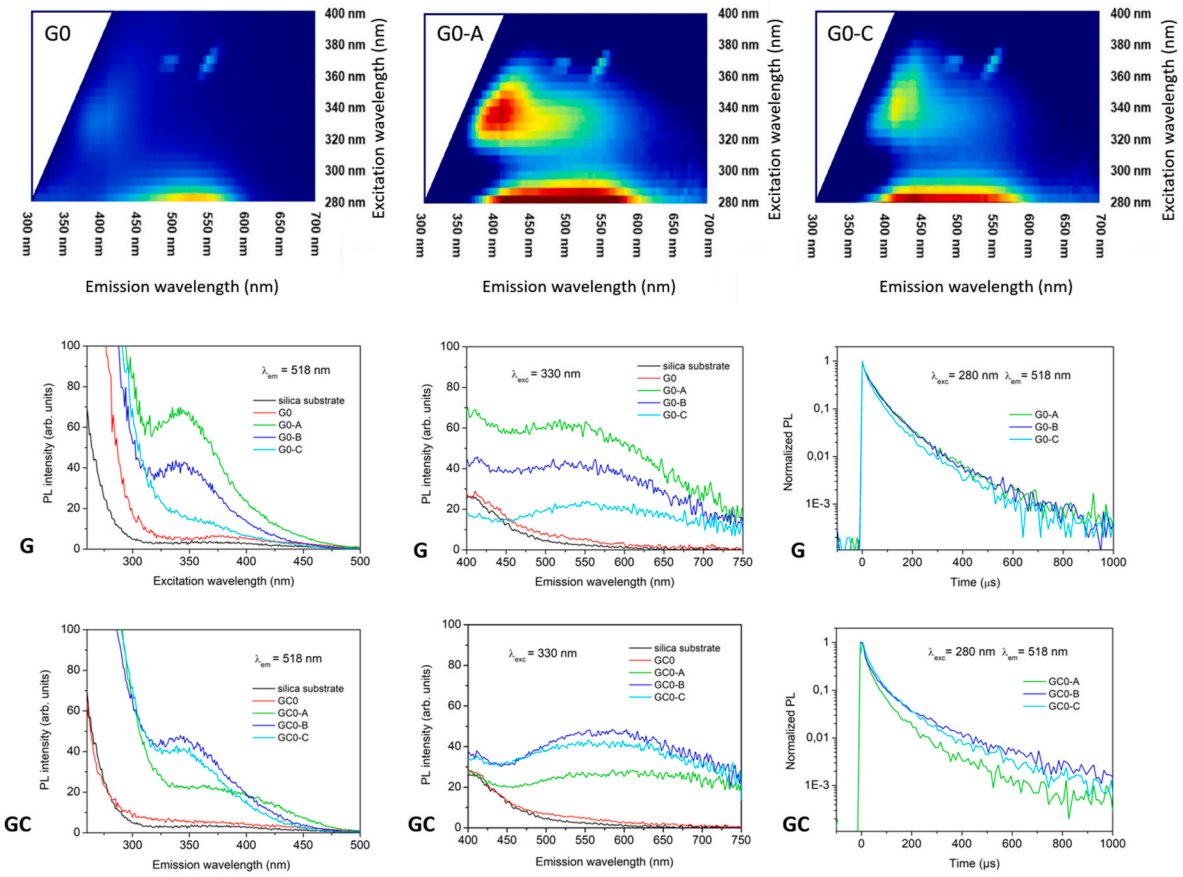

Fig. 5. PL excitation-emission maps for glassy samples G0 (without Ag), G0-A (as exchanged) and G0-C (exchanged and annealed at 430 °C). Ag nanoaggregates show a clear fingerprint with maximum peak excitation at about 340 nm and emission at about 410 nm (top row). PL excitation (left column: $\lambda_{em} = 518$ nm), PL emission (centre column: $\lambda_{exc} = 330$ nm) and time resolved PL spectra (right column: $\lambda_{exc} = 280$ nm, $\lambda_{em} = 518$ nm) of G (middle row) and GC (bottom row) samples indicate a different evolution with annealing temperature, which can be attributed to the different Ag mobility in the two environments.

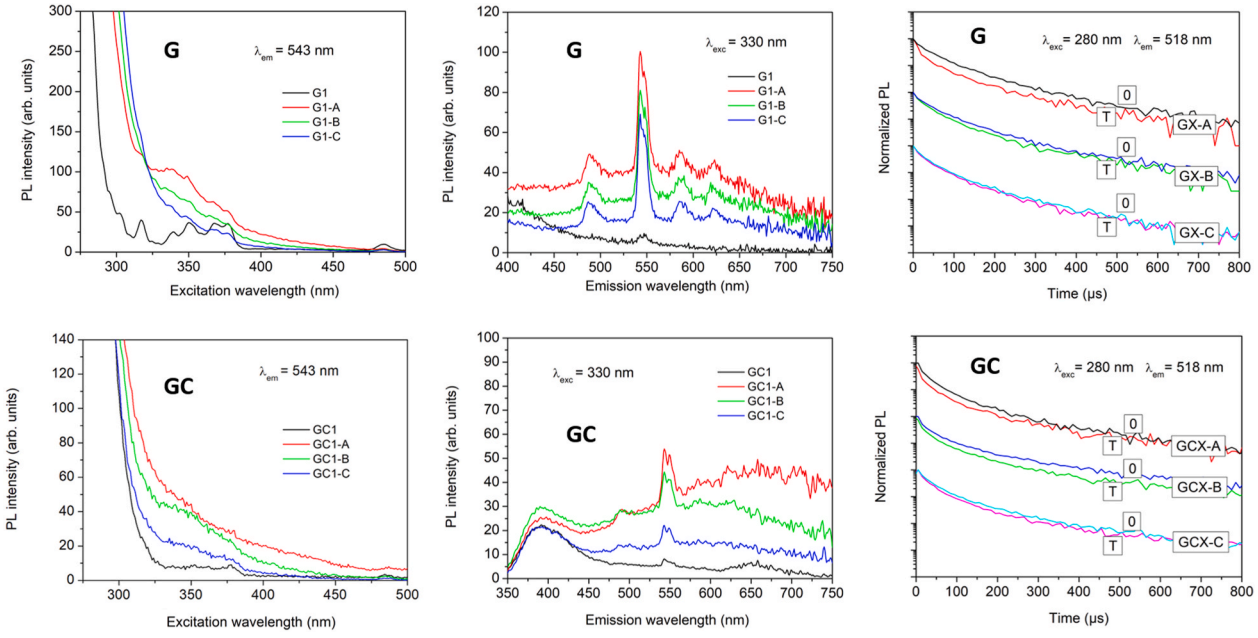

Fig. 6. PL excitation (left column: $\lambda_{em} = 543$ nm), PL emission (centre column: $\lambda_{exc} = 330$ nm) and time-resolved PL (right column: $\lambda_{exc} = 280$ nm, $\lambda_{em} = 518$ nm) of G (top row) and GC (bottom row) samples, indicating an efficient broadband enhanced excitation for Tb^{3+} ions after Ag exchange, both before and after annealing.

surrounding environment: the presence of non-radiative defects is responsible for additional recombination paths, with a reduction of the PL lifetime. For GC samples the thermal annealing results in a significant lifetime increase attesting a better optical quality of the material. This is already effective for annealing at 380 °C, without significant difference at 430 °C, in agreement with the previous discussion on the Ag mobility, that for GC samples would require much higher temperatures.

3.3. PL investigation of Ag–Tb^{3+} interaction (step II)

The interaction between silver aggregates and Tb^{3+} ions can be studied by PL excitation, emission and time-resolved spectroscopy. Before Ag-exchange, the typical spectroscopic features of Tb^{3+} doped samples are reported in Figure S4, representing the PLE (left, 543 nm emission) and PL (right, 280 nm excitation) of G1 and GC1 samples. The emission spectra, on the right, show the typical $^5D_4 \rightarrow {}^7F_J$ transitions of Tb^{3+} ions, with maximum peak at 543 nm associated to the $^5D_4 \rightarrow {}^7F_5$ transition. A significant difference can be highlighted between the two matrices, confirming the different local surroundings for the Tb^{3+} ions in G and GC materials: amorphous in the former and crystalline in the latter. On the left, the PLE spectra were obtained by monitoring the $^5D_4 \rightarrow {}^7F_5$ transition at 543 nm. The excitation of Tb^{3+} ions alone, without silver, can be obtained only by direct excitation of the rare earth ions or indirectly through charge transfer from the matrix. It should be noted that 330 nm excitation is not a very efficient excitation wavelength for Tb^{3+} ions, while it is very good for Ag nanoaggregates. However, as shown in Fig. 6, after Ag-exchange in the Tb-doped systems a significant increase of Tb^{3+} PL emission at 330 nm excitation can be detected, both in G and GC matrices (Table 1).

In glass, the enhancement rate $R_{Ag\text{-}Tb}$ of the peak area emission is about 12 times in G1-A (as-exchanged), 11 times in G1-B (exchanged and annealed at 380 °C) and 10 times in G1-C (exchanged and annealed at 430 °C). In glass-ceramics, the enhancement is 8 times in GC1-A, 6 times in GC1-B and 3 times in GC1-C samples. Moreover, the PLE graphs on the left of Fig. 6 show a clear improvement not only in the PL intensity but also in terms of excitation band, resulting in a broadband excitation which can cover the whole UV up to about 450 nm, resembling the PLE shape of Ag nanoaggregates discussed in the previous paragraph. This is a clear indication of the occurrence of an energy-transfer process from Ag nanoaggregates to Tb^{3+} ions, extremely interesting for solar cells and lighting applications, and in general for rare earth based optical devices which suffer from the low and narrow excitation cross section of RE^{3+} ions. Additionally, the time-resolved PL emission of Ag aggregates at 518 nm, a region not affected by Tb^{3+} emissions, is reported in the right column of Fig. 6 for Ag only doped and Ag–Tb co-doped G samples (G0-A,B,C and G1-A,B,C) and GC samples (GC0-A,B,C and GC1-A,B,C). All the samples exhibit a faster PL decay when co-doped by Tb^{3+} ions, as a further support for the energy-transfer process.

Table 1
Summary of the 543 nm Tb^{3+} PL intensity (background removed) at 330 nm excitation, the enhancement factors R, calculated as the intensity rate between the Tb^{3+} PL emissions with or without Ag aggregates, and the energy-transfer efficiencies η, calculated from Ag PL decay curves by using Eqn. (2).

Sample family	*PL (arb. units)* $\lambda_{exc} = 330$ nm $\lambda_{em} = 543$ nm	$R_{Ag\text{-}Tb}$ $\lambda_{exc} = 330$ nm	$\eta_{Ag\text{-}Tb}$ (%) $\lambda_{exc} = 280$ nm
G1	4.8	–	–
G1-A	59	12	38
G1-B	54	11	15
G1-C	50	10	9
GC1	2.8	–	–
GC1-A	22	8	32
GC1-B	16	6	29
GC1-C	8.4	3	9

PL investigation of Ag-Yb^{3+} and Ag–Tb^{3+}-Yb^{3+} interaction (step III).

A quantitative evaluation of the energy-transfer efficiency $\eta_{D\text{-}A}$ from a donor to an acceptor can be obtained by analysing the time-resolved PL decay of the donor emission (Ag nanoaggregates) without and with the acceptor (Tb^{3+} ions). This is a typical approach, since energy-transfer acts as an alternative non-radiative recombination path for the de-excitation of the sensitizer in co-doped samples, depleting the excited state. In other words, the number of emitted photons from the donor is reduced by the number of transferred excitations. The typical formula for describing this process is reported in Eqn. (2) hereafter:

$$\eta_{D-A} = 1 - \frac{\int I_{D-A} dt}{\int I_D dt} \quad (2)$$

The resulting energy-transfer efficiencies $\eta_{Ag\text{-}Tb}$ are reported in Table 1. It should be noted that they decrease after annealing, as well as the intensity enhancement rate $R_{Ag\text{-}Tb}$. It is worth highlighting that many factors could play a role in this process and a detailed quantitative analysis is not trivial. However, a similar behaviour was observed for other systems like in Si–Er co-doped glasses [51,52] and some qualitative trends can be drawn. First, annealing promotes the migration and aggregation of Ag atoms in multimers and clusters, as depicted previously. This has various important effects, which are discussed hereafter.

(a) Since the total amount of silver is determined by the ion-exchange process, increasing the size of Ag aggregates corresponds to a reduction of their total number and, consequently, of the enhancement efficiency.
(b) Connected with the previous point, the decrease of the number of sensitizers, and therefore of their density, corresponds to increasing the average distance between these donors (Ag species) and the acceptors (Tb^{3+} ions). In the general frame of a Förster-Dexter energy transfer process, the energy exchange may occur via a dipole-dipole interaction (Förster Resonance Energy Transfer, FRET) [53] or via an electron-transfer mechanism (Dexter) [54]. Both these non-radiative processes are strongly dependent on the distance, following a D^{-6} power law for the former and an exponential exp(-D) decrease for the latter. Typical distance range for FRET is 1–10 nm and for Dexter energy-transfer it is less than 1 nm. This last value is too short for being effective outside the scale length of a molecule, therefore only FRET may play a role in our system. Furthermore, when Ag nanoparticles are formed, plasmonic enhancement due to the concentrated electric field may also occur, which follows a similar exponential decrease, although introducing additional absorption losses. It might therefore be inferred, in agreement with our observations, that annealing could have a detrimental effect on the PL enhancement and transfer efficiency.
(c) Changing the nature of the sensitizers has the effect of modifying their optical properties, like the absorption cross section, and the electronic properties, such as the energy distribution of the electronic states, with a general PL downshifting. Since the efficiency of the Förster energy transfer process depends on the overlap of the electronic wavefunctions, which may be calculated as the integral overlap of the donor emission with the acceptor excitation, this aspect can play a crucial role on the transfer efficiency.
(d) Finally, annealing can improve the quality of the material reducing the presence of defects which might act as non-radiative recombination centres. This may increase the optical quantum efficiency of the system and allow for a better discrimination of the Förster energy transfer process.

The last link in the chain is the co-doping by Yb^{3+} ions, to provide NIR emission around 980 nm. Two possible mechanisms have been investigated (Fig. 1): the direct transfer from Ag aggregates to Yb^{3+} ions

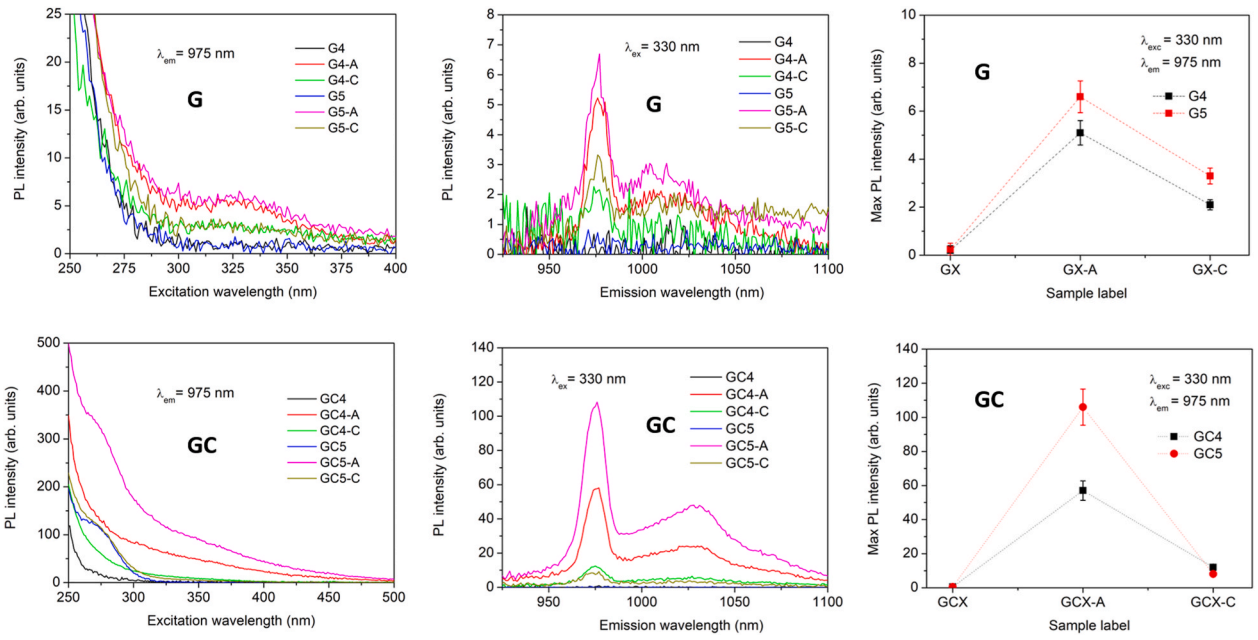

Fig. 7. PL excitation (left column: λ_{em} = 975 nm), PL emission (centre column: λ_{exc} = 330 nm) and maximum PL intensity (right column: λ_{exc} = 330 nm, λ_{em} = 975 nm) of G (top row) and GC (bottom row) samples, indicating an efficient broadband enhanced excitation for Yb^{3+} ions after Ag exchange.

(samples G4-A,B,C and GC4-A,B,C) and the transfer mediated by Tb^{3+} ions (samples G5-A,B,C and GC5-A,B,C), which could in principle provide a down-conversion mechanism. In Fig. 7 the PL excitation (left column, λ_{em} = 975 nm) and emission (centre column, λ_{exc} = 330 nm) for glass (top row) and glass-ceramic (bottom row) samples are reported.

Looking at the graphs, it can be noted that there is a significant difference between the samples with and without Ag. Indeed, Ag exchanged samples show a broadband excitation in the UV spectral region (left column), up to the violet and blue, which resemble the same Ag photoluminescence excitation seen in previous figures. Without Ag, the excitation spectra are flat down to about 300 nm. Below that wavelength, charge transfer from the matrix occurs. Ag sensitization allows for efficient RE^{3+} excitation also in regions where Tb^{3+} and Yb^{3+} are not able to absorb. Specifically, the NIR PL emission in the right column of Fig. 7 is shown for G (top) and GC (bottom) samples at 330 nm excitation, outside the wavelengths of direct excitation. Indeed, the corresponding spectra of G4/GC4 and G5/GC5 samples are completely flat, apart from noise, while the typical Yb^{3+} emissions, peaked at 976 nm, rise after Ag exchange. The effect is much stronger in GC samples, where the absolute PL intensities can be as much as 16 times higher with respect to G samples, even if the Ag amount is much lower, as detected by RBS analysis.

A limited role of Tb^{3+} ions in the G samples results in a slightly higher signal, without shape modification (both for PLE and PL spectra). This slight PL increase is reasonably attributed to the higher Ag concentration found in these samples, as discussed in the compositional analysis, rather than to a direct contribution from Tb^{3+} ions. Instead, a completely different situation can be highlighted for GC samples: in the PLE of GC samples, a specific fingerprint of Tb^{3+} ions can be seen, centred at about 270 nm. This feature is typical of Tb^{3+} ions in crystalline materials, associated with the charge transfer (CT) from the orbitals 2p of O^{2-} to the 4*f* of Tb^{3+} and with the intra-band allowed transitions 4*f*–5*d* of Tb^{3+} [55–59]. It has also been reported that the 4*f*–5*d* transition state of Tb^{3+} ions strongly depends on their environment and on the crystallite size [60]. Therefore, the PLE analysis on GC samples gives a strong indication of the role of both Ag nanoaggregates and Tb^{3+} ions in sensitizing Yb^{3+} ions, and a significant proof for the occurrence of a full-chain Ag–Tb-Yb energy transfer in the crystalline cubic zirconia environment. Finally, it should be noted that post-exchange annealing induces a significant decrease of the PL intensity both for G and GC samples.

A deeper investigation of the energy transfer process can be obtained by studying the combined PL emission from Ag aggregates and Tb^{3+} ions, which are both present at 543 nm, with or without Yb^{3+} co-doping. The PL analysis in terms of intensities and lifetimes is reported in Fig. 8 under 280 nm excitation. The graphs in the left column are examples of visible PL emissions, characterized by the presence of a broad background from Ag aggregates and specific transitions related to Tb^{3+} ions. Looking at the G samples, in the top row, we can observe that the PL intensities decrease after Yb^{3+} co-doping (central column), as expected when a transfer mechanism occurs, due to the depopulation of the emitting excited states. This is also confirmed by the strong lifetime reduction reported in the right column. By performing lifetime analysis according to Eqn. (2) the calculated transfer efficiencies are 54% (G1/G4), 41% (G1-A/G4-A), 72% (G1-B/G4-B), 52% (G1-C/G4-C). Although the significant efficiency of the energy transfer process in G samples, it is worth remembering that the effect is much stronger in GC samples, as discussed previously, with much higher PL intensities even if the Ag amount is much lower.

Furthermore, the comparison between G (top row) and GC (bottom row) samples with and without Yb^{3+} co-doping in Fig. 8 highlights a completely different behaviour: not only the visible PL intensities increase in glass ceramics, but also the PL lifetimes become longer, which may seem in contrast with the occurrence of an energy transfer process. However, as reported by XRD analysis (Fig. 3) and confirmed by the different Tb^{3+} spectral shape (Fig. 8, left bottom spectra), the presence of Yb has also a structural role, stabilizing the cubic zirconia phase against the tetragonal phase of undoped and Tb-only doped samples. According to theoretical and experimental analysis, the cubic phase has much lower phonon energies and higher symmetry than tetragonal or monoclinic phase [61]. Therefore, possible explanations for these differences relate to the different crystalline environment of GC which is more favourable to RE^{3+} ions, providing better spectroscopic properties than glass. In particular, the lower phonon energies of zirconia nanocrystals in glass-ceramics with respect to the glass matrix strongly reduce the occurrence of non-radiative recombinations, which are particularly detrimental in the NIR spectral region, explaining why the PL properties in the visible and in the NIR are so different for G and GC

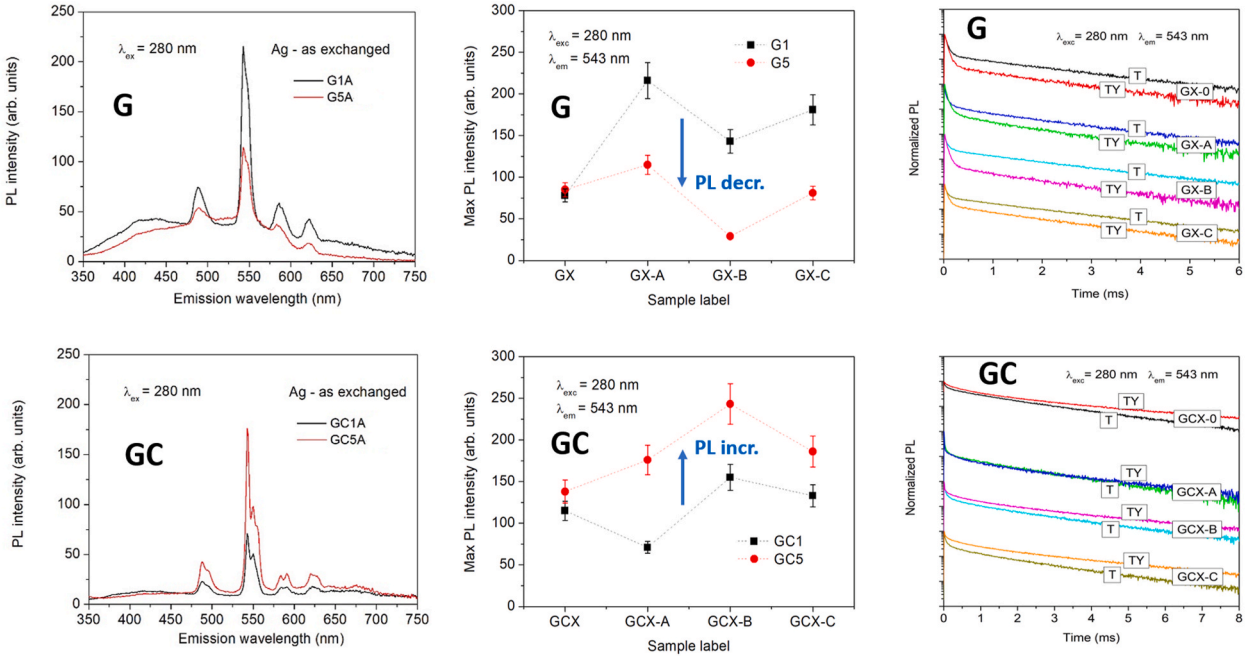

Fig. 8. Example of Ag–Tb^{3+} PL emission with and without Yb^{3+} co-doping (left column), comparison of the maximum PL intensity at 543 nm (central column – lines are only used as a help to viewer) and normalized time-resolved PL (right column) for the G (top row) and GC (bottom row) samples.

samples.

Additionally, it may be argued that GC matrix keeps a natural separation between Ag aggregates, dispersed in the multicomponent ion-exchanged glass phase, and RE^{3+} ions, localized mainly in the zirconia nanocrystals. This aspect can play a significant role, in analogy with similar mechanisms occurring in metallic particles, where surface enhanced fluorescence (SEF), known also as metal enhanced fluorescence (MEF), results from two competing processes: the amplification due to the local field and the non-radiative decay due to radiationless energy transfer [62–64]. The theoretical prediction of maximum SEF/-MEF for emitters located at a finite distance from the metal nanostructure has been experimentally confirmed by different research groups: Wokaun et al. (1983) [65], Aroca et al. [66], Novotny et al. [67], Lakowicz et al. [68,69], Halas et al. [70]. After a critical distance, the trend always mimics the near field intensity enhancement, $<|E|^2>$, as calculated by Mie theory. On the other hand, for any dipole emitter, at short distances from a metal surface, there is a giant enhancement of nonradiative decays due to Coulomb interaction with electrons in the metal. The combination of these two contributions agrees with the following Eqn. (3) [64]:

$$MEF(d) \approx \left|\frac{a}{a+d}\right|^6 - \left|\frac{1}{d}\right|^3 \quad (3)$$

Where "d" is the actual distance and "a" is defined as a critical distance, which can be obtained by theoretical calculations in each specific experiment, as discussed for example in the paper by Novotny et al. [67]. The maximum enhancement was obtained, in agreement with experiments, at a distance of about 5 nm. This value is perfectly matching the scale distance of our systems, where ZrO_2 tetragonal and cubic nanocrystals diameters are around 14 nm and 12 nm (broadly dispersed). However, we would expect that this effect plays a similar contribution on Tb^{3+} and Yb^{3+} ions, in contrast with our observations on visible and NIR PL emissions. Indeed, Tb^{3+} PL intensity is almost the same in the two environments, G and GC, while Yb^{3+} PL intensity is much higher in GC with respect to G samples, suggesting that this contribution, if present, is less important than the role attributed to the low phonon crystalline ZrO_2 phase.

4. Conclusion

This paper provides the first systematic and detailed investigation of the broadband Ag-sensitized downconversion process occurring in Tb^{3+}-Yb^{3+} codoped silica-zirconia glasses and glass-ceramics. Each link in the energy-transfer chain Ag-Tb^{3+}-Yb^{3+} has been analysed and discussed in relation to the compositional, structural and optical properties of the material. The differences between the amorphous and the crystalline environments have been highlighted. It was shown that, due to the higher mobility, Ag doping obtained by ion-exchange can be much higher in glasses (G) than in glass-ceramics (GC). Furthermore, significant rearrangement and surface migration was observed after thermal treatments only in G samples, without detectable modifications in GC samples. In addition, rare earth ions have an important structural role in determining the stabilization of a crystalline zirconia cubic phase in Yb^{3+} doped samples, while a tetragonal phase was observed for lower Tb^{3+} concentrations and for undoped samples. The sensitization role of Ag ions and multimers was clearly reported. In the visible spectral range, a one order of magnitude increase for Tb^{3+} PL intensity was measured, with an absolute intensity which is about three times higher in the glass than in the glass-ceramic. The energy-transfer quantum efficiency from Ag to Tb^{3+} was evaluated from lifetime measurements in 38% for the best G sample and 32% for the best GC sample. Instead, in the NIR spectral range the crystalline glass-ceramic matrix significantly overcomes the performance of the amorphous glass, in relation to the lower phonon energy and to the lower number of non-radiative defects. In both Ag-doped materials Yb^{3+} photoluminescence presents a broadband excitation up to 400 nm (G) and 500 nm (GC) spectral regions, which are completely ineffective without Ag due to the lack of specific energy levels, with an absolute PL intensity about 16 times higher in the glass-ceramic with respect to the glass. Finally, the energy-transfer process from Tb^{3+} to Yb^{3+} ions was demonstrated, as well as the possibility of a direct Ag-Yb^{3+} energy transfer, both in glasses and in glass ceramics, as a proof of working of the complete Ag-Tb^{3+}-Yb^{3+} chain for the first time, with efficiencies up to 78% in the glassy material.

In conclusion, our work clearly demonstrates that Ag ions, multimers and small aggregates can significantly boost the optical properties of Tb^{3+}-Yb^{3+} codoped materials both in the visible and in the NIR spectral

range, with great potential for light emitting devices and solar cells.

Declaration of competing interest

The authors declare that they have no known competing financial interests or personal relationships that could have appeared to influence the work reported in this paper.

Acknowledgements

D. Cristofori and T. Finotto of Ca' Foscari University of Venice (Italy) are acknowledged for support with SEM and TEM measurements respectively.

The research was partially funded by Centro Fermi through the MiFo project and the PLESC project (Ministero degli Affari Esteri e della Cooperazione Internazionale, MAECI) between South Africa and Italy. Francesco Enrichi acknowledges VINNOVA for financial support, under the Vinnmer Marie Curie Incoming – Mobility for Growth Programme (project "Nano2solar" Ref. N. 201602011), Alberto Vomiero acknowledges the Knut & Alice Wallenberg Foundation and the Kempe Foundation for financial support, the European Union's Horizon 2020 research and innovation programme under grant agreement No 654002 and INFN-LNL, Legnaro, Italy for RBS analyses.

Appendix A. Supplementary data

Supplementary data to this article can be found online at https://doi.org/10.1016/j.ceramint.2021.03.107.

References

[1] A. Meijerink, R. Wegh, P. Vergeer, T. Vlugt, Photon management with lanthanides, Opt. Mater. 28 (2006) 575–581, https://doi.org/10.1016/j.optmat.2005.09.055.
[2] T. Trupke, M.A. Green, P. Würfel, Improving solar cell efficiencies by down-conversion of high-energy photons, J. Appl. Phys. 92 (2002) 1668–1674, https://doi.org/10.1063/1.1492021.
[3] B.S. Richards, Luminescent layers for enhanced silicon solar cell performance: down-conversion, Sol. Energy Mater. Sol. Cells 90 (2006) 1189–1207, https://doi.org/10.1016/j.solmat.2005.07.001.
[4] G. Alombert-Goget, C. Armellini, S. Berneschi, A. Chiappini, A. Chiasera, M. Ferrari, S. Guddala, E. Moser, S. Pelli, D.N. Rao, G.C. Righini, Tb3+/Yb3+ co-activated Silica-Hafnia glass ceramic waveguides, Opt. Mater. 33 (2010) 227–230, https://doi.org/10.1016/j.optmat.2010.09.030.
[5] A. Bouajaj, S. Belmokhtar, M.R. Britel, C. Armellini, B. Boulard, F. Belluomo, A. Di Stefano, S. Polizzi, A. Lukowiak, M. Ferrari, F. Enrichi, Tb3+/Yb3+ codoped silica-hafnia glass and glass-ceramic waveguides to improve the efficiency of photovoltaic solar cells, Opt. Mater. 52 (2016) 62–68, https://doi.org/10.1016/j.optmat.2015.12.013.
[6] F. Enrichi, C. Armellini, S. Belmokhtar, A. Bouajaj, A. Chiappini, M. Ferrari, A. Quandt, G.C. Righini, A. Vomiero, L. Zur, Visible to NIR downconversion process in Tb3+-Yb3+codoped silica-hafnia glass and glass-ceramic sol-gel waveguides for solar cells, J. Lumin. 193 (2018) 44–50, https://doi.org/10.1016/j.jlumin.2017.08.027.
[7] G. Lakshminarayana, J. Qiu, Near-infrared quantum cutting in RE3+/Yb3+ (RE = Pr, Tb, and Tm): GeO2-B2O3-ZnO-LaF3 glasses via downconversion, J. Alloys Compd. 481 (2009) 582–589, https://doi.org/10.1016/j.jallcom.2009.03.034.
[8] X. Liu, S. Ye, Y. Qiao, G. Dong, B. Zhu, D. Chen, G. Lakshminarayana, J. Qiu, Cooperative downconversion and near-infrared luminescence of Tb3+-Yb3+ codoped lanthanum borogermanate glasses, Appl. Phys. B Laser Optic. 96 (2009) 51–55, https://doi.org/10.1007/s00340-009-3478-z.
[9] X. Zhou, Y. Wang, G. Wang, L. Li, K. Zhou, Q. Li, Cooperative downconversion and near-infrared luminescence of Tb 3+/Yb3+ co-doped tellurite glass, J. Alloys Compd. 579 (2013) 27–30, https://doi.org/10.1016/j.jallcom.2013.05.058.
[10] J.-L. Yuan, X.-Y. Zeng, J.-T. Zhao, Z.-J. Zhang, H.-H. Chen, X.-X. Yang, Energy transfer mechanisms in Tb3+ , Yb3+ codoped Y2O3 downconversion phosphor, J. Phys. D Appl. Phys. 41 (2008) 105406-1–105406-6, https://doi.org/10.1088/0022-3727/41/10/105406.
[11] A. Chiappini, L. Zur, F. Enrichi, B. Boulard, A. Lukowiak, G.C. Righini, M. Ferrari, Glass ceramics for frequency conversion, in: F. Enrichi, G.C. Righini (Eds.), Sol. Cells Light Manag. Mater. Strateg. Sustain., Elsevier, 2019.
[12] Y. Katayama, S. Tanabe, Downconversion for 1μm luminescence in lanthanide and Yb3+-codoped phosphors, in: F. Enrichi, G.C. Righini (Eds.), Sol. Cells Light Manag. Mater. Strateg. Sustain., Elsevier, 2019.
[13] S. Ye, Y. Katayama, S. Tanabe, Down conversion luminescence of Tb3+-Yb3+ codoped SrF2 precipitated glass ceramics, J. Non-Cryst. Solids 357 (2011) 2268–2271, https://doi.org/10.1016/j.jnoncrysol.2010.11.083.
[14] L. Zur, C. Armellini, S. Belmokhtar, A. Bouajaj, E. Cattaruzza, A. Chiappini, F. Coccetti, M. Ferrari, F. Gonella, G.C. Righini, E. Trave, A. Vomiero, F. Enrichi, Comparison between glass and glass-ceramic silica-hafnia matrices on the down-conversion efficiency of Tb3+/Yb3+ rare earth ions, Opt. Mater. 87 (2019) 102–106, https://doi.org/10.1016/j.optmat.2018.05.008.
[15] F. Auzel, Rare earth doped vitroceramics: new, efficient, blue and green emitting materials for infrared up-conversion, J. Electrochem. Soc. 122 (1975) 101–107, https://doi.org/10.1149/1.2134132.
[16] M. Mortier, A. Monteville, G. Patriarche, G. Maze, F. Auzel, New progresses in transparent rare-earth doped glass-ceramics, Opt. Mater. 16 (2001) 255–267, https://doi.org/10.1016/S0925-3467(00)00086-0.
[17] M.C. Gonçalves, L.F. Santos, R.M. Almeida, Rare-earth-doped transparent glass ceramics, Compt. Rendus Chem. 5 (2002) 845–854, https://doi.org/10.1016/S1631-0748(02)01457-1.
[18] E. Borsella, F. Gonella, P. Mazzoldi, A. Quaranta, G. Battaglin, R. Polloni, Spectroscopic investigation of silver in soda-lime glass, Chem. Phys. Lett. 284 (1998) 429–434, https://doi.org/10.1016/S0009-2614(97)01445-0.
[19] E. Borsella, E. Cattaruzza, G. De Marchi, F. Gonella, G. Mattei, P. Mazzoldi, A. Quaranta, G. Battaglin, R. Polloni, Synthesis of silver clusters in silica-based glasses for optoelectronics applications, J. Non-Cryst. Solids 245 (1999) 122–128, https://doi.org/10.1016/S0022-3093(98)00878-3.
[20] E. Borsella, G. Battaglin, M.A. Garcìa, F. Gonella, P. Mazzoldi, R. Polloni, A. Quaranta, Structural incorporation of silver in soda-lime glass by the ion-exchange process : a photoluminescence spectroscopy study, Appl. Phys. A 132 (2000) 125–132, https://doi.org/10.1007/PL00021106.
[21] E. Cattaruzza, M. Mardegan, E. Trave, G. Battaglin, P. Calvelli, F. Enrichi, F. Gonella, Modifications in silver-doped silicate glasses induced by ns laser beams, Appl. Surf. Sci. 257 (2011) 5434–5438, https://doi.org/10.1016/j.apsusc.2010.11.099.
[22] F. Enrichi, A. Quandt, G.C. Righini, Plasmonic enhanced solar cells: summary of possible strategies and recent results, Renew. Sustain. Energy Rev. 82 (2018) 2433–2439, https://doi.org/10.1016/j.rser.2017.08.094.
[23] G.C. Righini, B. Boulard, F. Coccetti, F. Enrichi, M. Ferrari, A. Lukowiakf, S. Pelli, L. Zur, A. Quandt, Light management in solar cells: recent advances, in: Int. Conf. Transparent Opt. Networks, 2017, pp. 1–6, https://doi.org/10.1109/ICTON.2017.8024832.
[24] H.A. Atwater, A. Polman, Plasmonics for improved photovoltaic devices, Nat. Mater. 9 (2010) 205–213, https://doi.org/10.1038/nmat2629.
[25] K.R. Catchpole, A. Polman, Plasmonic solar cells, Optic Express 16 (2008) 21793, https://doi.org/10.1364/OE.16.021793.
[26] J.-Y. Lee, P. Peumans, The origin of enhanced optical absorption in solar cells with metal nanoparticles embedded in the active layer, Optic Express 18 (2010) 10078, https://doi.org/10.1364/OE.18.010078.
[27] P. Spinelli, A. Polman, Prospects of near-field plasmonic absorption enhancement in semiconductor materials using embedded Ag nanoparticles, Optic Express 20 (2012) 641–654, https://doi.org/10.1364/OE.20.00A641.
[28] E. Cattaruzza, V.M. Caselli, M. Mardegan, F. Gonella, G. Bottaro, A. Quaranta, G. Valotto, F. Enrichi, Ag+↔Na+ion exchanged silicate glasses for solar cells covering: down-shifting properties, Ceram. Int. 41 (2015) 7221–7226, https://doi.org/10.1016/j.ceramint.2015.02.060.
[29] P. Mazzoldi, S. Padovani, F. Enrichi, G. Mattei, C. Sada, E. Trave, M. Guglielmi, A. Martucci, G. Battaglin, E. Cattaruzza, F. Gonella, C. Maurizio, Sensitizing effects in Ag-Er co-doped glasses for optical amplification, in: Proc. SPIE 5451, Integr. Opt. Photonic Integr. Circuits, 2004, pp. 311–326, https://doi.org/10.1117/12.549912.
[30] A. Martucci, M. De Nuntis, A. Ribaudo, M. Guglielmi, S. Padovani, F. Enrichi, G. Mattei, P. Mazzoldi, C. Sada, E. Trave, G. Battaglin, F. Gonella, E. Borsella, M. Falconieri, M. Patrini, J. Fick, Silver-sensitized erbium-doped ion-exchanged sol-gel waveguides, Appl. Phys. Mater. Sci. Process 80 (2005) 557–563, https://doi.org/10.1007/s00339-004-2967-5.
[31] E. Trave, M. Back, E. Cattaruzza, F. Gonella, F. Enrichi, T. Cesca, B. Kalinic, C. Scian, V. Bello, C. Maurizio, G. Mattei, Control of silver clustering for broadband Er3+luminescence sensitization in Er and Ag co-implanted silica, J. Lumin. 197 (2018) 104–111, https://doi.org/10.1016/j.jlumin.2018.01.025.
[32] F. Enrichi, C. Armellini, G. Battaglin, F. Belluomo, S. Belmokhtar, A. Bouajaj, E. Cattaruzza, M. Ferrari, F. Gonella, A. Lukowiak, M. Mardegan, S. Polizzi, E. Pontoglio, G.C. Righini, C. Sada, E. Trave, L. Zur, Silver doping of silica-hafnia waveguides containing Tb3+/Yb3+ rare earths for downconversion in PV solar cells, Opt. Mater. 60 (2016) 264–269, https://doi.org/10.1016/j.optmat.2016.07.048.
[33] F. Enrichi, S. Belmokhtar, A. Benedetti, A. Bouajaj, E. Cattaruzza, F. Coccetti, E. Colusso, M. Ferrari, P. Ghamgosar, F. Gonella, M. Karlsson, A. Martucci, R. Ottini, P. Riello, G.C. Righini, E. Trave, A. Vomiero, S. You, L. Zur, Ag nanoaggregates as efficient broadband sensitizers for Tb3+ ions in silica-zirconia ion-exchanged sol-gel glasses and glass-ceramics, Opt. Mater. 84 (2018) 668–674, https://doi.org/10.1016/j.optmat.2018.07.074.
[34] F. Enrichi, E. Cattaruzza, M. Ferrari, F. Gonella, R. Ottini, P. Riello, G.C. Righini, E. Trave, A. Vomiero, L. Zur, Ag-sensitized Yb3+ emission in glass-ceramics, Micromachines 9 (2018) 1–7, https://doi.org/10.3390/mi9080380.
[35] F. Enrichi, E. Cattaruzza, T. Finotto, P. Riello, G.C. Righini, E. Trave, A. Vomiero, Ag-sensitized NIR-emitting Yb3+-doped glass-ceramics, Appl. Sci. 10 (2020) 2184, https://doi.org/10.3390/app10062184.
[36] H. Lin, D. Chen, Y. Yu, R. Zhang, Y. Wang, Molecular-like Ag clusters sensitized near-infrared down-conversion luminescence in oxyfluoride glasses for broadband spectral modification, Appl. Phys. Lett. 103 (2013), 091902, https://doi.org/10.1063/1.4819951.

[37] F. Enrichi, E. Cattaruzza, M. Ferrari, F. Gonella, A. Martucci, R. Ottini, P. Riello, G. C. Righini, E. Trave, A. Vomiero, L. Zur, Investigation of the role of Ag multimers as broadband sensitizers in Tb3+/Yb3+ co-doped glass-ceramics, in: Proc. SPIE 10683. Fiber Lasers Glas, Photonics Mater. through Appl., 2018, p. 106830T, https://doi.org/10.1117/12.2314738.

[38] F. Gonella, Silver doping of glasses, Ceram. Int. 41 (2015) 6693–6701, https://doi.org/10.1016/J.CERAMINT.2015.02.058.

[39] L.R. Doolittle, Algorithms for the rapid simulation of Rutherford backscattering spectra, Nucl. Instrum. Methods Phys. Res. Sect. B Beam Interact. Mater. Atoms 9 (1985) 344–351, https://doi.org/10.1016/0168-583X(85)90762-1.

[40] S. Enzo, S. Polizzi, A. Benedetti, Applications of fitting techniques to the Warren-Averbach method for X-ray line broadening analysis, Z. Kristallogr. New Cryst. Struct. 170 (1985) 275–287, https://doi.org/10.1524/zkri.1985.170.1-4.275.

[41] A. Quaranta, E. Cattaruzza, F. Gonella, Modelling the ion exchange process in glass: phenomenological approaches and perspectives, Mater. Sci. Eng. B Solid-State Mater. Adv. Technol. 149 (2008) 133–139, https://doi.org/10.1016/j.mseb.2007.11.016.

[42] N.P. Bansal, R.H. Doremus, Handbook of Glass Properties, Academic Press, 2013, https://doi.org/10.1016/C2009-0-21785-5.

[43] P. Li, I.-W. Chen, J.E. Penner-Hahn, Effect of dopants on zirconia stabilization-an X-ray absorption study: I, trivalent dopants, J. Am. Ceram. Soc. 77 (1994) 118–128, https://doi.org/10.1111/j.1151-2916.1994.tb06964.x.

[44] P. Li, I.-W. Chen, J.E. Penner-Hahn, Effect of dopants on zirconia stabilization—an X-ray absorption study: II, tetravalent dopants, J. Am. Ceram. Soc. 77 (1994) 1281–1288, https://doi.org/10.1111/j.1151-2916.1994.tb05403.x.

[45] P. Li, I.-W. Chen, J.E. Penner-Hahn, Effect of dopants on zirconia stabilization—an X-ray absorption study: III, charge-compensating dopants, J. Am. Ceram. Soc. 77 (1994) 1289–1295, https://doi.org/10.1111/j.1151-2916.1994.tb05404.x.

[46] A. Sobolev, A. Musin, G. Whyman, K. Borodianskiy, O. Krichevski, A. Kalashnikov, M. Zinigrad, Stabilization of cubic phase in scandium-doped zirconia nanocrystals synthesized with sol-gel method, J. Am. Ceram. Soc. 102 (2019) 3236–3243, https://doi.org/10.1111/jace.16232.

[47] F.L. Cumbrera, G. Sponchia, A. Benedetti, P. Riello, J.M. Pérez-Mato, A.L. Ortiz, Some crystallographic considerations on the novel orthorhombic ZrO2 stabilized with Ta doping, Ceram. Int. 44 (2018) 10362–10366, https://doi.org/10.1016/j.ceramint.2018.03.048.

[48] X. Xu, J. Zhao, X. Luo, R. Ma, J. Qian, X. Qiao, J. Du, G. Qian, X. Zhang, X. Fan, Stabilization of fluorescent [Agm]n+ quantum clusters in multiphase inorganic glass-ceramics for white LEDs, ACS Appl. Nano Mater. 2 (2019) 2854–2863, https://doi.org/10.1021/acsanm.9b00312.

[49] I. Díez, R.H.A. Ras, Fluorescent silver nanoclusters, Nanoscale 3 (2011) 1963–1970, https://doi.org/10.1039/c1nr00006c.

[50] R. Ma, J. Zhao, X. Chen, X. Qiao, X. Fan, J. Du, X. Zhang, Stabilization of ultra-small [Ag2]2+ and [Ag:M]n+ nano-clusters through negatively charged tetrahedrons in oxyfluoride glass networks: to largely enhance the luminescence quantum yields, Phys. Chem. Chem. Phys. 19 (2017) 22638–22645, https://doi.org/10.1039/c7cp02531a.

[51] F. Enrichi, G. Mattei, C. Sada, E. Trave, D. Pacific, G. Franzò, F. Priolo, F. Iacona, M. Prassas, M. Falconieri, E. Borsella, Evidence of energy transfer in an aluminosilicate glass codoped with Si nanoaggregates and Er3+ ions, J. Appl. Phys. 96 (2004) 3925, https://doi.org/10.1063/1.1776637.

[52] F. Enrichi, G. Mattei, C. Sada, E. Trave, D. Pacifici, G. Franzò, F. Priolo, F. Iacona, M. Prassas, M. Falconieri, E. Borsella, Study of the energy transfer mechanism in different glasses co-doped with Si nanoaggregates and Er3+ ions, Opt. Mater. 27 (2005) 904–909, https://doi.org/10.1016/j.optmat.2004.08.033.

[53] T. Förster, Zwischenmolekulare Energiewanderung und Fluoreszenz, Ann. Phys. 437 (1948) 55–75, https://doi.org/10.1002/andp.19484370105.

[54] D.L. Dexter, A theory of sensitized luminescence in solids, J. Chem. Phys. 21 (1953) 836–850, https://doi.org/10.1063/1.1699044.

[55] R.E. Muenchausen, L.G. Jacobsohn, B.L. Bennett, E.A. McKigney, J.F. Smith, J. A. Valdez, D.W. Cooke, Effects of Tb doping on the photoluminescence of Y2O3:Tb nanophosphors, J. Lumin. 126 (2007) 838–842, https://doi.org/10.1016/j.jlumin.2006.12.004.

[56] Q. Meng, B. Chen, W. Xu, Y. Yang, X. Zhao, W. Di, S. Lu, X. Wang, J. Sun, L. Cheng, T. Yu, Y. Peng, Size-dependent excitation spectra and energy transfer in Tb3+ -doped Y2 O3 nanocrystalline, J. Appl. Phys. 102 (2007), 093505, https://doi.org/10.1063/1.2803502.

[57] M. Back, A. Massari, M. Boffelli, F. Gonella, P. Riello, D. Cristofori, R. Riccò, F. Enrichi, Optical investigation of Tb3+-doped Y2O3 nanocrystals prepared by Pechini-type sol-gel process, J. Nanoparticle Res. 14 (2012) 792, https://doi.org/10.1007/s11051-012-0792-x.

[58] I. Ahemen, F.B. Dejene, R. Botha, Strong green-light emitting Tb3+ doped tetragonal ZrO2 nanophosphors stabilized by Ba2+ ions, J. Lumin. 201 (2018) 303–313, https://doi.org/10.1016/j.jlumin.2018.05.003.

[59] S.K. Gupta, P.S. Ghosh, A.K. Yadav, N. Pathak, A. Arya, S.N. Jha, D. Bhattacharyya, R.M. Kadam, Luminescence properties of SrZrO3/Tb3+ perovskite: host-dopant energy-transfer dynamics and local structure of Tb3+, Inorg. Chem. 55 (2016) 1728–1740, https://doi.org/10.1021/acs.inorgchem.5b02639.

[60] G. Blasse, G.C. Grabmaier, Luminescent Materials, Springer-Verlag Berlin Heidelberg (Germany), 1994, https://doi.org/10.1007/978-3-642-79017-1.

[61] X. Zhao, D. Vanderbilt, Phonons and lattice dielectric properties of zirconia, Phys. Rev. B Condens. Matter 65 (2002), 075105, https://doi.org/10.1103/PhysRevB.65.075105.

[62] C.D. Geddes, J.R. Lakowicz, Metal-enhanced fluorescence, J. Fluoresc. 12 (2002) 121–129, https://doi.org/10.1023/A:1016875709579.

[63] J.R. Lakowicz, Principles of Fluorescence Spectroscopy, Springer-Verlag, Boston (MA), USA, 2006, https://doi.org/10.1007/978-0-387-46312-4.

[64] R.F. Aroca, Plasmon enhanced spectroscopy, Phys. Chem. Chem. Phys. 15 (2013) 5355–5363, https://doi.org/10.1039/c3cp44103b.

[65] A. Wokaun, H.P. Lutz, A.P. King, U.P. Wild, R.R. Ernst, Energy transfer in surface enhanced luminescence, J. Chem. Phys. 79 (1983) 509–514, https://doi.org/10.1063/1.445550.

[66] R. Aroca, G.J. Kovacs, C.A. Jennings, R.O. Loutfy, P.S. Vincett, Fluorescence enhancement from Langmuir-blodgett monolayers on silver island films, Langmuir 4 (1988) 518–521, https://doi.org/10.1021/la00081a004.

[67] P. Anger, P. Bharadwaj, L. Novotny, Enhancement and quenching of single-molecule fluorescence, Phys. Rev. Lett. 96 (2006) 1–4, https://doi.org/10.1103/PhysRevLett.96.113002.

[68] K. Ray, R. Badugu, J.R. Lakowicz, Distance-dependent metal-enhanced fluorescence from Langmuir-Blodgett monolayers of Alkyl-NBD derivatives on silver island films, Langmuir 22 (2006) 8374–8378, https://doi.org/10.1021/la061058f.

[69] N. Akbay, J.R. Lakowicz, K. Ray, Distance-dependent metal-enhanced intrinsic fluorescence of proteins using polyelectrolyte layer-by-layer assembly and aluminum nanoparticles, J. Phys. Chem. C 116 (2012) 10766–10773, https://doi.org/10.1021/jp2122714.

[70] R. Bardhan, N.K. Grady, N.J. Halas, Nanoscale control of near-infrared fluorescence enhancement using Au nanoshells, Small 4 (2008) 1716–1722, https://doi.org/10.1002/smll.200800405.